

ARMY RESEARCH LABORATORY



Fluid Simulation of Klystron Output Cavities With Optimization of Electron Beam Bunching

Alan Bromborsky

ARL-TR-2097

June 2000

Approved for public release; distribution unlimited.

20000727 165

The findings in this report are not to be construed as an official Department of the Army position unless so designated by other authorized documents.

Citation of manufacturer's or trade names does not constitute an official endorsement or approval of the use thereof.

Destroy this report when it is no longer needed. Do not return it to the originator.

Army Research Laboratory

Adelphi, MD 20783-1197

ARL-TR-2097

June 2000

Fluid Simulation of Klystron Output Cavities With Optimization of Electron Beam Bunching

Alan Bromborsky

Sensors and Electron Devices Directorate

Abstract

A one-dimensional fluid model for a coupled system of klystron output cavities is developed. The model is exercised for both realistic and optimized beam current modulation waveforms, and the rf conversion efficiency is calculated. An optimized second harmonic velocity modulation and associated current modulation are calculated and inputted into the cavity simulation. Optimum bunching lengths and rf conversion efficiencies are determined.

Contents

1	Introduction	1
2	Klystron Output Cavity System	2
2.1	Multiplet Output Cavity System	2
2.2	Driven-Mode Equations	3
2.3	Space-Charge Fields	5
2.4	Fluid Equations	6
2.5	Finite Element Expansion	7
2.6	Basis Selection for Finite Element Formulation	10
2.7	Calculation of rf and Beam Kinetic Power	12
2.8	Output Cavity Operation with Specified Current Modulation	13
3	Efficiency Enhancement by Harmonic Bunching	19
3.1	Current Modulation for Arbitrary Velocity Modulation . . .	19
3.2	Optimized Velocity Modulation	22
3.3	Effect of Harmonic Bunching Upon Output Cavity Efficiency	24
4	Conclusions	28
	References	29
	Distribution	31
	Report Documentation Page	33

Figures

1	Doublet output cavity	2
2	Power convergence for 20-kW beam with sinusoidal velocity modulation	16
3	Diagnostics for efficiency-optimized buncher cavity with sinusoidal velocity-modulated 20-kW beam	16
4	Power convergence for 2-MW beam with sinusoidal velocity modulation	16
5	Diagnostics for efficiency-optimized buncher cavity with sinusoidal velocity-modulated 2-MW beam	17
6	Power convergence for 20-kW beam with 25 percent duty factor gate current modulation	17
7	Diagnostics for efficiency-optimized buncher cavity with 25 percent duty factor current-modulated 20-kW beam	17
8	Power convergence for 2-MW beam with 25 percent duty factor gate current modulation	18
9	Diagnostics for efficiency-optimized buncher cavity with 25 percent duty factor current-modulated 2-MW beam	18
10	Current modulation for electron beam with sinusoidal velocity modulation at $z = 0.7, 0.8, 0.9$, and 1.0 of optimum drift distance z_0	21
11	Current modulation for electron beam with optimized velocity modulation at $z = 0.7, 0.8, 0.9$, and 0.99 of optimum drift distance z_0	23
12	Current modulation for electron beam with second harmonic approximation $\beta_{[2]}(\varphi)$ to optimized velocity modulation at drift length z_0	24
13	Comparison of current modulation at z_0 for sinusoidal velocity modulation	24
14	Power convergence for 20-kW beam with optimized second harmonic velocity modulation and output cavity gap located at $z = z_0$	25

15	Diagnostics for efficiency-optimized buncher cavity with optimized second harmonic velocity-modulated 20-kW beam and output cavity gap located at $z = z_0$	26
16	Power convergence for 2-MW beam with optimized second harmonic velocity modulation and output cavity gap located at $z = 0.9z_0$	26
17	Power convergence for 20-kW beam with optimized second harmonic velocity modulation and output cavity gap located at $z = 0.9z_0$	26

Tables

1	Summary of output cavity simulation results for 10- μ perv electron beam	14
2	Parameters for bunching calculations	21
3	Summary of output cavity simulation results for 10- μ perv electron beam with second harmonic ballistic bunching . . .	27

1. Introduction

Klystron-like (klystron, multibeam klystron, reltron, RKA) rf (radio frequency) sources are very suitable for high-peak and average-power microwave applications, including directed energy warfare (DEW). This suitability is due to a configuration in which the electron beam collector is separate from the rf generation cavities (unlike the magnetron or crossed field amplifier (CFA)). Because of this separation, heating in the rf cavities is due only to conduction currents flowing in the cavity wall and not to electrons impinging on the walls of the rf cavities (if the tube is correctly designed). The major deficiencies of klystron-like rf sources (compared to magnetrons and CFAs) are a relatively high operating voltage and a significantly lower efficiency. In this report, I address the problem of high voltage in a klystron-like device by using a high perveance ($>10 \mu\text{perv}$) electron beam as is done in the multibeam klystron amplifier. The problem of increasing the klystron efficiency centers on the particular current modulation impressed upon the electron beam. To determine an achievable electron beam modulation that will maximize the klystron efficiency while minimizing the number of cavities and hence the length of the klystron, I have developed a fast one-dimensional fluid simulation of a klystron output cavity. This simulation will allow me to perform a comprehensive parametric study on the beam modulation required to maximize the rf conversion efficiency of the klystron. After the optimum current modulation is determined, a realizable velocity modulation that will produce an approximation to the optimum current modulation is derived, and the rf conversion efficiency for such a current modulation is determined with the fluid simulation. In particular, the optimum ballistic bunching distance for the derived velocity modulation is determined with the fluid simulation from a parametric study.

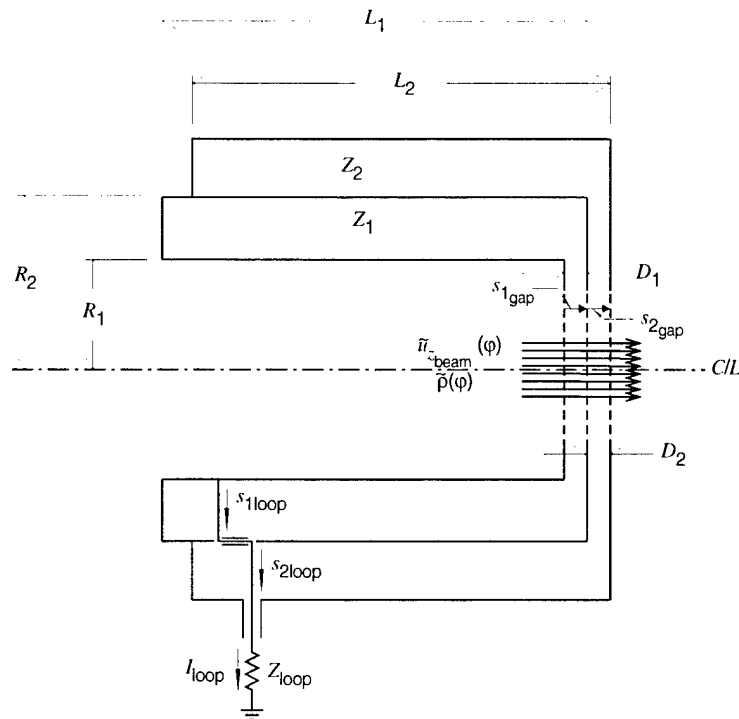
2. Klystron Output Cavity System

2.1 Multiplet Output Cavity System

The purpose of the klystron output (or multiplet output) cavity system is to efficiently convert the kinetic energy in the current-modulated electron beam into rf power. An example of an output cavity system that is analogous to the doublet buncher cavity [1] is shown in figure 1. The only differences in the configuration of the buncher and the output cavities is that in the output cavity, no generator is in series with the load impedance and the electron beam entering the cavity is highly current modulated.

As in a previous paper that analyzed the buncher cavity [1], I will analyze the general case of a multiplet output cavity system. Unlike the buncher cavity, a single-harmonic time analysis would not be useful for the output cavity. First, because of the nature of ballistic focusing, the current modulation of the electron beam entering the output cavity system is very rich in higher harmonics. Second, since current gains (over the current injected

Figure 1. Doublet output cavity. (Variable will be explained later in report.)



into the buncher cavity) of greater than 20 are achievable, the peak current in the output cavity system could approach the static-limiting current for the cavity gap. In the output cavity system, the effects of both space-charge and higher-order cavity modes must be considered. The space-charge effects may increase the efficiency of the output cavity by transferring energy from the higher-current harmonics to the fundamental frequency.

2.2 Driven-Mode Equations

In the output cavity system, the current distribution driving the cavity is not guaranteed to be sinusoidal in time. To account for this situation, I must use the general expression for the amplitude $c_{l,k}(t)$ of the l th driven mode in the k th cavity of an N cavity output cavity system. The following equation (1) is the same as equation (7) in a previous paper [1], but with $V_{\text{gen}} = 0$, Z_{gen} replaced by Z_{load} , and the gap and loop voltages in each cavity being the sum of the gap and loop voltages of the fundamental cavity mode ($l = 0$) and the higher harmonic modes ($1 \leq l \leq N_k$) in the k th cavity:

$$\ddot{c}_{l,k}(t) + \omega_{l,k}^2 c_{l,k}(t) = \frac{i\omega_{l,k}}{\epsilon_0 \int_{\Omega_k} dV |\mathcal{E}_{l,k}(\mathbf{x}_k)|^2} \left\{ i \frac{V_{l,k}^* \text{loop}}{Z_{\text{load}}} \sum_{m=1}^N \sum_{n=0}^{N_m} \frac{\dot{c}_{n,m}(t)}{\omega_{n,m}} V_{n,m} \text{loop} - \int_{\Omega_k} dV \mathcal{E}_{l,k}^*(\mathbf{x}_k) \cdot \mathbf{J}_k(\mathbf{x}_k, t) \right\}. \quad (1)$$

Now I introduce the phase variable $\varphi = \omega t$, where ω is the drive frequency of the buncher cavity. While I cannot expect $c_{l,k}(t)$ to be sinusoidal in time, I can assume that it will achieve a periodic equilibrium with period $2\pi/\omega$. With this change of variable, let $\tilde{z}_k = z_k/D_k$ and $\tilde{\omega}_{l,k} = \omega_{l,k}/\omega$, so that the driven mode equations become

$$\frac{d^2 c_{l,k}}{d\varphi^2} + \tilde{\omega}_{l,k}^2 c_{l,k} = \frac{i\tilde{\omega}_{l,k}}{\omega \epsilon_0 \int_{\Omega_k} dV |\mathcal{E}_{l,k}(\mathbf{x}_k)|^2} \left\{ i \frac{V_{l,k}^* \text{loop}}{Z_{\text{load}}} \sum_{m=1}^N \sum_{n=0}^{N_m} \frac{1}{\tilde{\omega}_{n,m}} \frac{dc_{n,m}}{d\varphi} V_{n,m} \text{loop} - \int_{\Omega_k} dV \mathcal{E}_{l,k}^*(\mathbf{x}_k) \cdot \mathbf{J}_k(\mathbf{x}_k, \varphi) \right\}, \quad (2)$$

$$\frac{d^2 c_{l,k}}{d\varphi^2} + \tilde{\omega}_{l,k}^2 c_{l,k} = i\tilde{\omega}_{l,k} \Delta \tilde{\omega}_{l,k} \left\{ i \sum_{m=1}^N \sum_{n=0}^{N_m} \frac{1}{\tilde{\omega}_{n,m}} \frac{V_{n,m} \text{loop}}{V_{l,k} \text{loop}} \frac{dc_{n,m}}{d\varphi} - \frac{Z_{\text{load}}}{|V_{l,k} \text{loop}|^2} \int_{\Omega_k} dV \mathcal{E}_{l,k}^*(\mathbf{x}_k) \cdot \mathbf{J}_k(\mathbf{x}_k, \varphi) \right\}, \quad (3)$$

$$\frac{d^2 c_{l,k}}{d\varphi^2} + \tilde{\omega}_{l,k}^2 c_{l,k} = i\tilde{\omega}_{l,k} \Delta \tilde{\omega}_{l,k} \left\{ \begin{aligned} & i \sum_{m=1}^N \sum_{n=0}^{N_m} \frac{1}{\tilde{\omega}_{n,m}} \frac{V_{n,m \text{ loop}}}{V_{l,k \text{ loop}}} \frac{dc_{n,m}}{d\varphi} \\ & - \frac{\pi R_b^2 Z_{\text{load}}}{V_{l,k \text{ loop}}} \frac{V_{l,k \text{ gap}}^*}{V_{l,k \text{ loop}}^*} \int_0^1 d\tilde{z}_k J_{z_k}(\tilde{z}_k, \varphi) \end{aligned} \right\}. \quad (4)$$

The system of $\sum_{k=1}^N N_k$ equations described by equation (4) is of a second order and thus is not suitable for a solution (when coupled to the electron fluid) by standard ordinary differential equation solvers (Runge-Kutta, etc). I will convert equation (4) to a system of $2\sum_{k=1}^N N_k$ first order differential equations by introducing the variables $V_{l,k}$. These variables are the driven gap voltages for the l th mode of the k th gap in the multiplet output cavity system. The relationship between $V_{l,k}$ and $c_{l,k}$ is given by

$$\frac{V_{l,k}}{D_k} = -\frac{i}{\omega_{l,k}} \frac{V_{l,k \text{ gap}}}{D_k} \dot{c}_{l,k}(t). \quad (5)$$

The additional $\sum_{k=1}^N N_k$ first order equations required to complete the system are

$$\frac{d}{d\varphi} (V_{l,k \text{ gap}} c_{l,k}) = i\tilde{\omega}_{l,k} V_{l,k}. \quad (6)$$

Using equation (6) to eliminate the second derivative from equation (4) gives

$$\frac{dV_{l,k}}{d\varphi} = i\tilde{\omega}_{l,k} (V_{l,k \text{ gap}} c_{l,k}) \quad (7)$$

$$- \Delta \tilde{\omega}_{l,k} \left\{ \begin{aligned} & \frac{V_{l,k \text{ gap}}}{V_{l,k \text{ loop}}} \sum_{m=1}^N \sum_{n=0}^{N_m} \frac{V_{n,m \text{ loop}}}{V_{n,m \text{ gap}}} V_{n,m} \\ & + \pi R_b^2 Z_{\text{load}} \left| \frac{V_{l,k \text{ gap}}}{V_{l,k \text{ loop}}} \right|^2 \int_0^1 d\tilde{z}_k J_{z_k}(\tilde{z}_k, \varphi) \end{aligned} \right\} \quad \text{and}$$

$$\frac{dV_{l,k}}{d\varphi} = i\tilde{\omega}_{l,k} (V_{l,k \text{ gap}} c_{l,k}) \quad (8)$$

$$- \Delta \tilde{\omega}_{l,k} \left\{ \begin{aligned} & G_{l,k} \sum_{m=1}^N \sum_{n=0}^{N_m} \frac{V_{n,m}}{G_{n,m}} \\ & + \pi R_b^2 Z_{\text{load}} |G_{l,k}|^2 \int_0^1 d\tilde{z}_k J_{z_k}(\tilde{z}_k, \varphi) \end{aligned} \right\}.$$

Now I introduce the dimensionless variables $\tilde{V}_{l,k}$ and $\tilde{c}_{l,k}$ defined by

$$\tilde{V}_{l,k} = \frac{V_{l,k}}{V_{\text{norm}_k}} \quad \text{and} \quad (9)$$

$$\tilde{c}_{l,k} = i \frac{V_{l,k \text{ gap}}}{V_{\text{norm}_k}} c_{l,k}, \quad (10)$$

so that the dimensionless first order driven-mode equations become

$$\frac{d\tilde{c}_{l,k}}{d\varphi} = -\tilde{\omega}_{l,k}\tilde{V}_{l,k}, \quad \text{and} \quad (11)$$

$$\frac{d\tilde{V}_{l,k}}{d\varphi} = \tilde{\omega}_{l,k}\tilde{c}_{l,k} - \Delta\tilde{\omega}_{l,k} \left\{ G_{l,k} \sum_{m=1}^N \sum_{n=0}^{N_m} \frac{\tilde{V}_{n,m}}{G_{n,m}} + \frac{\pi R_b^2 Z_{\text{load}}}{V_{\text{norm}_k}} |G_{l,k}|^2 \int_0^1 d\tilde{z}_k \rho_k(\tilde{z}_k, \varphi) u_{z_k}(\tilde{z}_k, \varphi) \right\}. \quad (12)$$

I shall leave the normalization constant V_{norm_k} undefined for now so that I can select a value for it later that will lead to the greatest simplification of the fluid equations. Note that for a lossless cavity, $\tilde{\omega}_{l,k}$, $\Delta\tilde{\omega}_{l,k}$, and $G_{l,k}$ will be real and the system of equations describing the electron beam cavity system will be real.

2.3 Space-Charge Fields

For the k th planar gap, Poisson's equation is

$$\frac{d^2\varphi_k}{dz_k^2} = -\frac{\rho_k(z_k, \varphi)}{\epsilon_0}. \quad (13)$$

The same equation with a normalized position variable (\tilde{z}_k) becomes

$$\frac{d^2\varphi_k}{d\tilde{z}_k^2} = -\frac{D_k^2 \rho_k(\tilde{z}_k, \varphi)}{\epsilon_0}, \quad (14)$$

with boundary conditions $\varphi_k(0) = \varphi_k(1) = 0$. Equation (14) can be directly integrated, giving

$$\frac{d\varphi_k}{d\tilde{z}_k} = -\frac{D_k^2}{\epsilon_0} \int_0^{\tilde{z}_k} d\tilde{z}' \rho_k(\tilde{z}', \varphi) + \left. \frac{d\varphi_k}{d\tilde{z}_k} \right|_0 \quad (15)$$

$$\varphi_k = -\frac{D_k^2}{\epsilon_0} \int_0^{\tilde{z}_k} d\tilde{z}' \int_0^{\tilde{z}'} d\tilde{z}'' \rho_k(\tilde{z}'', \varphi) + \tilde{z}_k \left. \frac{d\varphi_k}{d\tilde{z}_k} \right|_0 + \varphi_k(0) \quad (16)$$

$$\varphi_k(1) = -\frac{D_k^2}{\epsilon_0} \int_0^1 d\tilde{z}' \int_0^{\tilde{z}'} d\tilde{z}'' \rho_k(\tilde{z}'', \varphi) + \left. \frac{d\varphi_k}{d\tilde{z}_k} \right|_0 + \varphi_k(0) \quad (17)$$

$$\left. \frac{d\varphi_k}{d\tilde{z}_k} \right|_0 = \frac{D_k^2}{\epsilon_0} \int_0^1 d\tilde{z}' \int_0^{\tilde{z}'} d\tilde{z}'' \rho_k(\tilde{z}'', \varphi) \quad (18)$$

$$\varphi_k = \frac{D_k^2}{\epsilon_0} \left(\tilde{z}_k \int_0^1 d\tilde{z}' \int_0^{\tilde{z}'} d\tilde{z}'' \rho_k(\tilde{z}'', \varphi) - \int_0^{\tilde{z}_k} d\tilde{z}' \int_0^{\tilde{z}'} d\tilde{z}'' \rho_k(\tilde{z}'', \varphi) \right) \quad (19)$$

$$-\nabla\varphi_k = -\frac{1}{D_k} \frac{d\varphi_k}{d\tilde{z}_k} = \frac{D_k}{\epsilon_0} \left(\int_0^{\tilde{z}_k} d\tilde{z}' \rho_k(\tilde{z}', \varphi) - \int_0^1 d\tilde{z}' \int_0^{\tilde{z}'} d\tilde{z}'' \rho_k(\tilde{z}'', \varphi) \right). \quad (20)$$

Equation (20) gives the contribution of the space charge electric field to the total electric field.

2.4 Fluid Equations

The fluid equations for the k th planar cavity gap (l th cavity mode excited) are

$$\frac{\partial \rho_k}{\partial t} + \rho_k \frac{\partial u_{z_k}}{\partial z_k} + u_{z_k} \frac{\partial \rho_k}{\partial z_k} = 0 \quad \text{and} \quad (21)$$

$$\frac{\partial u_{z_k}}{\partial t} + u_{z_k} \frac{\partial u_{z_k}}{\partial z_k} = -\frac{e}{m} \left(\frac{1}{D_k} \sum_{n=0}^{N_k} V_{n,k} + \frac{d\varphi_k}{dz_k} \right). \quad (22)$$

Transforming equations (21) and (22) into ones that will use the dimensionless variables φ and \tilde{z}_k gives

$$\omega \frac{\partial \rho_k}{\partial \varphi} + \frac{\rho_k}{D_k} \frac{\partial u_{z_k}}{\partial \tilde{z}_k} + \frac{u_{z_k}}{D_k} \frac{\partial \rho_k}{\partial \tilde{z}_k} = 0 \quad \text{and} \quad (23)$$

$$\omega \frac{\partial u_{z_k}}{\partial \varphi} + \frac{u_{z_k}}{D_k} \frac{\partial u_{z_k}}{\partial \tilde{z}_k} = -\frac{e}{m} \left(\frac{1}{D_k} \sum_{n=0}^{N_k} V_{n,k} + \frac{1}{D_k} \frac{d\varphi_k}{d\tilde{z}_k} \right). \quad (24)$$

Substituting equation (20) into equation (24) gives

$$\begin{aligned} \omega \frac{\partial u_{z_k}}{\partial \varphi} + \frac{u_{z_k}}{D_k} \frac{\partial u_{z_k}}{\partial \tilde{z}_k} = & -\frac{e}{m} \left[\frac{1}{D_k} \sum_{n=0}^{N_k} V_{l,k} \right. \\ & \left. - \frac{D_k}{\epsilon_0} \left(\int_0^{\tilde{z}_k} d\tilde{z}' \rho_k(\tilde{z}', \varphi) - \int_0^1 d\tilde{z}' \int_0^{\tilde{z}'} d\tilde{z}'' \rho_k(\tilde{z}'', \varphi) \right) \right]. \end{aligned} \quad (25)$$

Making equation (23) dimensionless requires that

$$\tilde{u}_{z_k} = \frac{u_{z_k}}{\omega D_k} \quad (26)$$

and then equation (23) becomes

$$\frac{\partial \rho_k}{\partial \varphi} + \rho_k \frac{\partial \tilde{u}_{z_k}}{\partial \tilde{z}_k} + \tilde{u}_{z_k} \frac{\partial \rho_k}{\partial \tilde{z}_k} = 0. \quad (27)$$

The form of equation (27) allows ρ_k to be normalized in any way to simplify equation (25). First I write equation (25) with the chosen u_{z_k} normalization (eq (26)) to show how to normalize ρ_k :

$$\frac{\partial \tilde{u}_{z_k}}{\partial \varphi} + \tilde{u}_{z_k} \frac{\partial \tilde{u}_{z_k}}{\partial \tilde{z}_k} = -\frac{e}{m} \left[\frac{1}{\omega^2 D_k^2} \sum_{n=0}^{N_k} V_{n,k} - \frac{1}{\omega^2 \epsilon_0} \left(\int_0^{\tilde{z}_k} d\tilde{z}' \rho_k(\tilde{z}', \varphi) - \int_0^1 d\tilde{z}' \int_0^{\tilde{z}'} d\tilde{z}'' \rho_k(\tilde{z}'', \varphi) \right) \right]. \quad (28)$$

By inspecting equation (28), I see the correct normalizations are

$$V_{\text{norm}_k} = -\frac{\omega^2 m D_k^2}{e} = -\frac{mc^2}{e} \left(\frac{\omega D_k}{c} \right)^2 \quad \text{and} \quad (29)$$

$$\tilde{\rho}_k = -\frac{e \rho_k}{m \omega^2 \epsilon_0} = -\frac{e Z_0}{mc \left(\frac{\omega}{c} \right)^2} \rho_k. \quad (30)$$

These equations transform equations (27) and (28) into

$$\frac{\partial \tilde{\rho}_k}{\partial \varphi} + \tilde{\rho}_k \frac{\partial \tilde{u}_{z_k}}{\partial \tilde{z}_k} + \tilde{u}_{z_k} \frac{\partial \tilde{\rho}_k}{\partial \tilde{z}_k} = 0 \quad \text{and} \quad (31)$$

$$\frac{\partial \tilde{u}_{z_k}}{\partial \varphi} + \tilde{u}_{z_k} \frac{\partial \tilde{u}_{z_k}}{\partial \tilde{z}_k} = \sum_{n=0}^{N_k} \tilde{V}_{n,k} + \int_0^{\tilde{z}_k} d\tilde{z}' \tilde{\rho}_k - \int_0^1 d\tilde{z}' \int_0^{\tilde{z}'} d\tilde{z}'' \tilde{\rho}_k. \quad (32)$$

A normalized load impedance \tilde{Z}_{L_k} is defined by

$$\tilde{Z}_{L_k} = \frac{\pi \omega R_b^2 Z_{\text{load}}}{c D_k Z_0}, \quad (33)$$

so that equation (12) becomes

$$\frac{d \tilde{V}_{l,k}}{d \varphi} = \tilde{\omega}_{l,k} \tilde{c}_{l,k} - \Delta \tilde{\omega}_{l,k} \times \left(G_{l,k} \sum_{m=1}^N \sum_{n=0}^{N_m} \frac{\tilde{V}_{n,m}}{G_{n,m}} + \tilde{Z}_{L_k} |G_{l,k}|^2 \int_0^1 d\tilde{z}_k \tilde{\rho}_k \tilde{u}_{z_k} \right), \quad (34)$$

and the system that must be solved for determining the performance of the output cavity consists of equations (11), (31), (32), and (34).

2.5 Finite Element Expansion

To solve the output cavity equations with the use of finite element method, the first step is to expand $\tilde{u}_{z_k}(\tilde{z}_k, \varphi)$ and $\tilde{\sigma}_k(\tilde{z}_k, \varphi)$ as a set of at least once differentiable axial basis functions $s_m^k(\tilde{z}_k)$. Note that in subsequent formulas, N_{z_k} denotes the number of axial basis functions for the k th gap. The basis functions must be differentiable at least once, since I am solving a

system of first-order equations. I am also restricting the basis functions to be real to speed up the numerics of the solution process. The finite element expansions for the velocity and charge density fields are

$$\tilde{u}_{z_k}(\tilde{z}_k, \varphi) = \sum_{m=1}^{N_{z_k}} \tilde{u}_{z_k.m}(\varphi) s_m^k(\tilde{z}_k) \quad \text{and} \quad (35)$$

$$\tilde{\rho}_k(\tilde{z}_k, \varphi) = \sum_{m=1}^{N_{z_k}} \tilde{\rho}_{k.m}(\varphi) s_m^k(\tilde{z}_k). \quad (36)$$

In the following equations, prime when applied to a function will denote differentiation. Second, I define the auxillary basis functions as

$$t_m^k(\tilde{z}_k) = \int_0^{\tilde{z}_k} d\tilde{z}'_k s_m^k(\tilde{z}'_k), \quad (37)$$

and the dyadic matrixes as

$$A_{lm}^k = \int_0^1 d\tilde{z}_k s_l^k(\tilde{z}_k) s_m^k(\tilde{z}_k), \quad (38)$$

$$B_l^k = \int_0^1 d\tilde{z}_k s_l^k(\tilde{z}_k), \quad (39)$$

$$C_{lmn}^k = \int_0^1 d\tilde{z}_k s_l^k(\tilde{z}_k)' s_m^k(\tilde{z}_k) s_n^k(\tilde{z}_k) - s_l^k(1) s_m^k(1) s_n^k(1), \quad (40)$$

$$D_{lm}^k = \int_0^1 d\tilde{z}_k s_l^k(\tilde{z}_k) t_m^k(\tilde{z}_k), \quad \text{and} \quad (41)$$

$$E_l^k = \int_0^1 d\tilde{z}_k t_l^k(\tilde{z}_k). \quad (42)$$

Then the third step is to reduce equation (34) by noting that the finite element expansion allows me to substitute

$$\int_0^1 d\tilde{z}_k \tilde{\rho}_k \tilde{u}_{z_k} = \sum_{m=1}^{N_{z_k}} \sum_{n=1}^{N_{z_k}} A_{mn}^k \tilde{\rho}_{k.m} \tilde{u}_{z_k.n}, \quad (43)$$

giving

$$\frac{d\tilde{V}_{l,k}}{d\varphi} = \tilde{\omega}_{l,k} \tilde{c}_{l,k} - \Delta \tilde{\omega}_{l,k} \times \left(G_{l,k} \sum_{m=1}^N \sum_{n=0}^{N_m} \frac{\tilde{V}_{n,m}}{G_{n,m}} + \tilde{Z}_{L_k} |G_{l,k}|^2 \sum_{m=1}^{N_{z_k}} \sum_{n=1}^{N_{z_k}} A_{mn}^k \tilde{\rho}_{k.m} \tilde{u}_{z_k.n} \right). \quad (44)$$

This is the only effect of the finite element expansion upon the cavity equations. Now I will reduce the charge conservation equation to its finite element equivalent. First I rewrite equation (31) as

$$\frac{\partial \tilde{\rho}_k}{\partial \varphi} + \frac{\partial(\tilde{u}_{z_k} \tilde{\rho}_k)}{\partial \tilde{z}_k} = 0. \quad (45)$$

Next I multiply equation (45) by $s_l^k(\tilde{z}_k)$ and integrate from 0 to 1 by

$$\int_0^1 d\tilde{z}_k s_l^k \left(\frac{\partial \tilde{\rho}_k}{\partial \varphi} + \frac{\partial(\tilde{u}_{z_k} \tilde{\rho}_k)}{\partial \tilde{z}_k} \right) = 0 . \quad (46)$$

Substituting equations (35) and (36) and integrating by parts give

$$\int_0^1 d\tilde{z}_k s_l^k s_m^k \frac{d\tilde{\rho}_{k,m}}{d\varphi} + \left[s_l^k \tilde{u}_{z_k} \tilde{\rho}_k \right]_0^1 - \int_0^1 d\tilde{z}_k \left(s_l^k \right)' \tilde{\rho}_k \tilde{u}_{z_k} = 0 . \quad (47)$$

Using the definitions for A_{lm}^k and C_{lmn}^k reduces the finite element approximation of the charge conservation equation to

$$\sum_{m=1}^{N_{z_k}} A_{lm}^k \frac{d\tilde{\rho}_{k,m}}{d\varphi} = \sum_{m=1}^{N_{z_k}} \sum_{n=1}^{N_{z_k}} C_{lmn}^k \tilde{\rho}_{k,m} \tilde{u}_{z_{k,n}} + s_l^k(0) \tilde{J}_k(0, \varphi) = 0 . \quad (48)$$

The reduction of equation (32) (fluid equation) proceeds in a like manner:

$$\begin{aligned} \int_0^1 d\tilde{z}_k s_l^k \left(\frac{\partial \tilde{u}_{z_k}}{\partial \varphi} + \frac{1}{2} \frac{\partial \tilde{u}_{z_k}^2}{\partial \tilde{z}_k} \right) &= \int_0^1 d\tilde{z}_k s_l^k \left(\sum_{n=0}^{N_k} \tilde{V}_{n,k} \right) \\ &+ \int_0^1 d\tilde{z}_k s_l^k \int_0^{\tilde{z}_k} d\tilde{z}' \tilde{\rho}_k - \int_0^1 d\tilde{z}_k s_l^k \int_0^1 d\tilde{z}' \int_0^{\tilde{z}'} d\tilde{z}'' \tilde{\rho}_k . \end{aligned} \quad (49)$$

Treating each part of equation (49) separately gives the following finite element expansions:

$$\begin{aligned} \int_0^1 d\tilde{z}_k s_l^k \left(\frac{\partial \tilde{u}_{z_k}}{\partial \varphi} + \frac{\partial \tilde{u}_{z_k}^2}{\partial \tilde{z}_k} \right) &= \sum_{m=1}^{N_{z_k}} A_{lm}^k \frac{d\tilde{u}_{z_{k,m}}}{d\varphi} \\ &- \sum_{m=1}^{N_{z_k}} \sum_{n=1}^{N_{z_k}} C_{lmn}^k \tilde{u}_{z_{k,m}} \tilde{u}_{z_{k,n}} - \frac{1}{2} s_l^k(0) \tilde{u}_{z_k}(0, \varphi)^2 , \end{aligned} \quad (50)$$

$$\int_0^1 d\tilde{z}_k s_l^k \left(\sum_{n=0}^{N_k} \tilde{V}_{n,k} \right) = B_l^k \left(\sum_{n=0}^{N_k} \tilde{V}_{n,k} \right) , \quad (51)$$

$$\int_0^1 d\tilde{z}_k s_l^k \int_0^{\tilde{z}_k} d\tilde{z}' \tilde{\rho}_k = \sum_{m=1}^{N_{z_k}} D_{lm}^k \tilde{\rho}_{k,m} , \quad \text{and} \quad (52)$$

$$\int_0^1 d\tilde{z}_k s_l^k \int_0^1 d\tilde{z}' \int_0^{\tilde{z}'} d\tilde{z}'' \tilde{\rho}_k = B_l^k \sum_{m=1}^{N_{z_k}} E_m^k \tilde{\rho}_{k,m} . \quad (53)$$

Substituting equations (50), (51), (52), and (53) into equation (49) gives the finite element form of the fluid equation,

$$\sum_{m=1}^{N_{z_k}} A_{lm}^k \frac{d\tilde{u}_{z_k,m}}{d\varphi} = \frac{1}{2} \sum_{m=1}^{N_{z_k}} \sum_{n=1}^{N_{z_k}} C_{lmn}^k \tilde{u}_{z_k,m} \tilde{u}_{z_k,n} + \frac{1}{2} s_l^k(0) \tilde{u}_{z_k}(0, \varphi)^2 B_l^k \left(\sum_{n=0}^{N_k} \tilde{V}_{n,k} + \sum_{m=1}^{N_{z_k}} E_m^k \tilde{\rho}_{k,m} \right) - \sum_{m=1}^{N_{z_k}} D_{lm}^k \tilde{\rho}_{k,m} . \quad (54)$$

Finally, the boundary conditions on the beam velocity and current density fields are given by equations (55) and (56) for $k \geq 1$:

$$\tilde{u}_{z_k}(0, \varphi) = \sum_{m=1}^{N_{z_{k-1}}} s_m^{k-1}(1) \tilde{u}_{z_{k,k-1,m}}(\varphi) \quad \text{and} \quad (55)$$

$$\tilde{J}_k(0, \varphi) = \tilde{u}_{z_k}(0, \varphi) \sum_{m=1}^{N_{z_{k-1}}} s_m^{k-1}(1) \tilde{\rho}_{k,k-1,m}(\varphi) . \quad (56)$$

For $k = 0$, the beam modulation functions $\tilde{u}_{z_0}(0, \varphi)$ and $\tilde{J}_0(0, \varphi)$ are either assumed or calculated from the ballistic bunching equations.

2.6 Basis Selection for Finite Element Formulation

The basis functions selected for the finite element formulation should allow for efficient evaluation of the derivatives in equations (11), (44), (48), and (54) so that a standard differential equation solver, such as Runge-Kutta, can be used to solve the system. Additionally, the basis functions should be in a form such that relatively few functions are required to approximate the velocity and charge distributions. Since some of the current modulation waveforms that will be used to model the electron beam injected into the output gap have large derivatives, the basis functions must be able to model charge densities that have a rapid spatial variation. Because of this property, basis functions consisting of $e^{\pm 2\pi i l \tilde{z}}$ were not considered, since large values of l would be required to model rapidly varying functions. In the end, I selected the basis set for the piecewise linear functions. If the interval $[0, 1]$ of the k th output gap is partitioned into N_{z_k} intervals by the grid $\{\tilde{z}_{k0}, \dots, \tilde{z}_{k1}, \dots, \tilde{z}_{kN_{z_k}}\}$, where $\tilde{z}_{k0} = 0$ and $\tilde{z}_{kN_{z_k}} = 1$, the N_{z_k} piecewise linear basis functions defined by this grid are

$$s_1^k(\tilde{z}_k) = \begin{cases} 1 - \frac{\tilde{z}_k}{\tilde{z}_{k1}} & 0 \leq \tilde{z}_k \leq \tilde{z}_{k1} \\ 0 & \tilde{z}_{kN_{z_k-1}} < \tilde{z}_k \leq 1 \end{cases} , \quad (57)$$

$$s_l^k(\tilde{z}_k) = \begin{cases} 0 & 0 \leq \tilde{z}_k \leq \tilde{z}_{k_{l-1}} \\ \frac{\tilde{z}_k - \tilde{z}_{k_{l-1}}}{\tilde{z}_{k_l} - \tilde{z}_{k_{l-1}}} & \tilde{z}_{k_{l-1}} < \tilde{z}_k \leq \tilde{z}_{k_l} \\ \frac{\tilde{z}_{k_{l+1}} - \tilde{z}_k}{\tilde{z}_{k_{l+1}} - \tilde{z}_{k_l}} & \tilde{z}_{k_l} \leq \tilde{z}_k < \tilde{z}_{k_{l+1}} \\ 0 & \tilde{z}_{k_{l+1}} \leq \tilde{z}_k \leq 1 \end{cases}, \quad \text{and} \quad (58)$$

$$s_{N_{z_k}}^k(\tilde{z}_k) = \begin{cases} 0 & 0 \leq \tilde{z}_k < \tilde{z}_{k_{N_{z_k}-1}} \\ 1 - \frac{1 - \tilde{z}_k}{1 - \tilde{z}_{k_{N_{z_k}-1}}} & \tilde{z}_{k_{N_{z_k}-1}} \leq \tilde{z}_k \leq 1 \end{cases}, \quad (59)$$

so that an arbitrary function $f^k(\tilde{z}_k)$ that takes on the values $f^k(\tilde{z}_{k_l}) = f_l^k$ in the k th output gap may be represented by

$$f^k(\tilde{z}_k) = \sum_{l=1}^{N_{z_k}} f_l^k s_l^k(\tilde{z}_k). \quad (60)$$

This choice of basis results in sparse arrays for A_{mn}^k and C_{lmn}^k and a triangular array for D_{mn}^k . All arrays are evaluated using a C++ class library for piecewise polynomial functions. First the basis set

$$\{s_l^k(\tilde{z}_k), \quad 1 \leq l \leq N_{z_k}\} \quad (61)$$

is defined as an array of piecewise linear functions. This array of functions is then integrated (one of the standard operations for the class) to generate the associated array

$$\{t_l^k(\tilde{z}_k), \quad 1 \leq l \leq N_{z_k}\} \quad (62)$$

of piecewise quadratic functions. Then the functions in the arrays are appropriately multiplied to form the piecewise polynomial functions (quadratic and cubic) that are the integrands in equations 38 through 42. Multiplication of piecewise polynomial functions is also a standard class operation. The integrals are then analytically evaluated (another standard class operation). The piecewise polynomial class library simplifies evaluating the required arrays for any set of basis functions that are piecewise polynomials.

From a computational point of view, the selected basis set is very attractive since the array A_{mn}^k is a tridiagonal matrix. This property allows rapid evaluation of the derivatives in the finite element equations with the use of standard algorithms [2, p 50], even though the basis functions are not orthogonal (A_{mn}^k is not diagonal).

Once I selected the basis functions and evaluated the finite element arrays, the next step was to solve the system of coupled nonlinear differential equations defined by the equations (11), (44), (48), and (54). The method selected was the Cash-Karp variation of the Runge-Kutta method, with adaptive step size control [2, p 717]. This method is very robust, can deal with rapidly varying functions, and will optimize the step size of the integration. This method was implemented as a C++ virtual base class, with the derived class supplying the required derivative functions to the differential equation solver base class.

2.7 Calculation of rf and Beam Kinetic Power

The whole purpose of the klystron is to produce rf power. The output cavity is where the rf is extracted from the klystron. To calculate the rf power extracted, one needs to calculate the load current, which is also the loop current, $I_{\text{loop}}(t)$. This is given by

$$I_{\text{loop}}(t) = \frac{i}{Z_{\text{load}}} \sum_{k=1}^N \sum_{n=0}^{N_k} \frac{\dot{c}_{n,k}(t)}{\omega_{n,k}} V_{n,k \text{ loop}} , \quad (63)$$

$$I_{\text{loop}}(\varphi) = \frac{i}{Z_{\text{load}}} \sum_{k=1}^N \sum_{n=0}^{N_k} \frac{1}{\tilde{\omega}_{n,k}} \frac{dc_{n,k}}{d\varphi} V_{n,k \text{ loop}} , \quad \text{and} \quad (64)$$

$$I_{\text{loop}}(\varphi) = \frac{mc^2}{eZ_{\text{load}}} \sum_{k=1}^N \left(\frac{\omega D_k}{c} \right)^2 \sum_{n=0}^{N_k} \frac{\tilde{V}_{n,k}}{G_{n,k}} . \quad (65)$$

The rf power averaged over one rf cycle is then

$$\langle P_{\text{rf}} \rangle = \frac{\omega Z_{\text{load}}}{2\pi} \int_0^{2\pi} dt I_{\text{loop}}(t)^2 \quad \text{and} \quad (66)$$

$$\langle P_{\text{rf}} \rangle = \frac{Z_{\text{load}}}{2\pi} \int_0^{2\pi} d\varphi I_{\text{loop}}(\varphi)^2 . \quad (67)$$

Since the load current can have significant harmonic content, I performed a Fourier expansion of $I_{\text{loop}}(\varphi)$ and calculated the power associated with each harmonic to determine the harmonic power spectrum of the klystron for each drive frequency, ω .

Since I used approximate models to determine the behavior of the output cavity system, I needed to implement diagnostic tests to determine if the fundamental conservation laws are being obeyed by our approximate model. To do this, I needed to calculate the average electron beam kinetic power at the exit of the output gap. The kinetic power density of a one-dimensional fluid is given by

$$\frac{dP_{\text{ke}}}{dS} = \frac{1}{2} \left(\frac{m}{e} \right) \rho_z u_z^3 . \quad (68)$$

For a beam of radius R_b , the instantaneous beam kinetic power at the output of the k th output gap is

$$P_{ke}^k(1) = \frac{\pi R_b^2}{2} \left(\frac{m}{e} \right) \rho_k(1) u_{z_k}(1)^3 = \frac{\pi}{2Z_0} (k_0 R_b)^2 (k_0 D_k)^3 \left(\frac{mc^2}{e} \right)^2 \tilde{\rho}_k(1) \tilde{u}_{z_k}(1)^3, \quad (69)$$

where $k_0 = \omega/c$. Define

$$P_N = \frac{1}{Z_0} \left(\frac{mc^2}{e} \right)^2 = 0.69313 \text{ GW} \quad (70)$$

as the power normalization. The average beam kinetic power during one rf cycle is then

$$\langle P_{ke}^k(1) \rangle = \frac{P_N}{4} (k_0 R_b)^2 (k_0 D_k)^3 \int_0^{2\pi} d\varphi \tilde{\rho}_k(1, \varphi) \tilde{u}_{z_k}(1, \varphi)^3. \quad (71)$$

With the use of the normalizing power defined in equation (70), the rf power becomes

$$\langle P_{rf} \rangle = \frac{P_N}{2\pi} \left(\frac{Z_0}{Z_{load}} \right) \int_0^{2\pi} d\varphi \left(\sum_{k=1}^N (k_0 D_k)^2 \sum_{n=0}^{N_k} \frac{\tilde{V}_{n,k}}{G_{n,k}} \right)^2, \quad (72)$$

and the conservation law is

$$\langle P_{ke}^0(0) \rangle = \lim_{\varphi \rightarrow \infty} \{ \langle P_{rf} \rangle + \langle P_{ke}^N(1) \rangle \}. \quad (73)$$

Equation (73) states that after oscillatory equilibrium is reached, the average kinetic power of the beam entering the multiplet output cavity is equal to the sum of average rf power to the multiplet output cavity load and the average kinetic power of the beam exiting the multiplet output cavity. This is a statement of conservation of energy. Averages over equilibrium rf cycles must be used because of the energy stored in the cavity and space charge fields.

2.8 Output Cavity Operation with Specified Current Modulation

After being coded, the fluid simulation of the output cavity was run for the modulation and electron beam parameters shown in table 1. The ballistic current modulation referenced in table 1 is for a standard two-cavity klystron, where a buncher gap imparts a small (5 percent) velocity modulation to the electron beam, and the beam is then drifted over a distance that will provide optimum beam bunching. The equations describing this

Table 1. Summary of output cavity simulation results for 10- μ perv electron beam. No ballistic drift length associated with 25 percent gate modulation. A 5 percent velocity modulation is assumed for a ballistically generated current modulation.

Modulation	Drift length (cm)	Beam power	Voltage (kV)	Current (A)	Efficiency
Ballistic	25	20 kW	5.25	3.8	0.560
Ballistic	63	2 MW	33.14	60.3	0.565
25% gate	—	20 kW	5.25	3.8	0.894
25% gate	—	2 MW	33.14	60.3	0.896

type of current modulation and the numerical equivalent of the treatment [3, p 300] are given in section 3.1 of this report. The 25 percent gate current modulation is simply imposed on the electron beam entering the output cavity with the peak beam current normalized so that the average beam power for both types of current modulation is the same. The modulation is trapezoidal in time with rise and fall times that are 5 percent of the full-width-half-maximum (FWHM) duration of the pulse while the FWHM duration is 25 percent of an rf cycle. For all the cases treated in this report, the rf frequency is 1 GHz with an rf cycle time of 1 ns. Once I selected the modulation and the beam parameters (voltage and perveance), I ran the code for several instances of beam loading (combination of gap gain and load impedance). For each run, the system was stepped forward in time until it achieved oscillatory equilibrium or until the electron velocity field became negative at some location leading to electron trajectory crossing. This criterion was used because the fluid model was only applicable if the electron trajectories **within the buncher cavity gap** did not cross. If oscillatory equilibrium was achieved, the beam loading was increased until oscillatory equilibrium was no longer possible; then the beam loading was slightly decreased until oscillatory equilibrium returned. This value of beam loading is considered to be optimum—it results in the maximum efficiency for the conversion of beam kinetic energy to rf power.

A summary of the code runs is shown in table 1 with the detailed results displayed in figures 2 through 9. Figures 2, 4, 6, and 8 show both the input beam current and velocity modulations ($I_b(0)$ and $\beta_z(0)$ in the small graph on the right side of the figures), the average (over one rf cycle) rf power $\langle P_{rf} \rangle$ and beam kinetic power $\langle P_{ke} \rangle$, and the minimum value of the velocity field in the cavity gap during the rf cycle, $\min(\beta_z)$. Currently, the cavities are assumed to have a simple transmission line geometry as in figure 1 so that the eigen modes can be calculated with a simple analytic expression. Figures 3, 5, 7, and 9 show the detailed behavior of the beam current $I_b(1)$ and beam velocity $\beta_z(1)$ modulation at the output of the cavity gap. Additionally, the voltages across both the load V_{load} and cavity gap V_{gap} are shown.

The most striking of the results shown in table 1 is that a simple 25 percent duty factor trapezoidal beam current modulation produces a significantly higher conversion of electron beam kinetic power to rf power than the standard ballistic electron beam current modulation. This effect is independent of beam power. The 2-MW beams have the same conversion efficiencies as the 20-kW beams with the same modulation waveforms. The explanation of this effect can be found by comparing the beam current and velocity fields in figures 3 and 7. In figure 3 when $(\pi/2 < \varphi < 3\pi/2)$, the current at the cavity output is small, and the beam velocity is large. When the velocity is small, the beam current is large. However, if I compare the beam current under similar conditions as shown in figures 3 and 7, the beam current in figure 7 is much closer to zero for large values of beam velocity compared to the beam current in figure 3. The modulation used in figure 7 gives a much higher efficiency than the standard optimum ballistic modulation, because the modulated beam current entering the output cavity is zero for almost 75 percent of an rf cycle. For the trapezoidal modulation, all the electrons in the beam slow down and give up energy to the rf field. For the ballistic modulation, the beam current is never truly zero and a significant number of the electrons entering the output cavity will have a phase that causes them to be accelerated by the rf field in the cavity, reducing the rf output power. To increase the efficiency of the klystron, I must decrease the modulated beam current for those phases that allow acceleration of the electrons. The next section of this report develops a method for implementing such a modulation.

Before moving on, one numerical aspect of the fluid simulation requires some commentary. Note that on the trailing edges of the modulated current $I_b(0)$ exiting the output cavity (figs. 3, 5, 7, and 9), the current changes sign. Since I do not allow the velocity field to become negative, the only way for the current to change sign is for the charge density field to change sign. But this cannot physically happen since I have a fluid consisting only of electrons. The current changes sign because of the limitations of the approximating functions in the finite element expansion (a Gibbs phenomenon). If the number of approximating functions is increased, the frequency of the negative current oscillations is also increased, and the oscillations decay more rapidly. Also note that the oscillations for the trapezoidal current modulation are not as great as for the optimum sinusoidal velocity modulation. This is because the $dI_b/d\varphi$ entering the output cavity is smaller for the trapezoidal current modulation. One should not worry about this discrepancy, since the fluid simulation is only one step in a multilayer approach to klystron design and analysis. After achieving a fluid model optimized klystron, one should use the optimized fluid model as a starting point for the more detailed particle-in-cell (PIC) model of the electron beam.

Figure 2. Power convergence for 20-kW beam with sinusoidal velocity modulation. Equilibrium efficiency is $\eta = 0.56$.

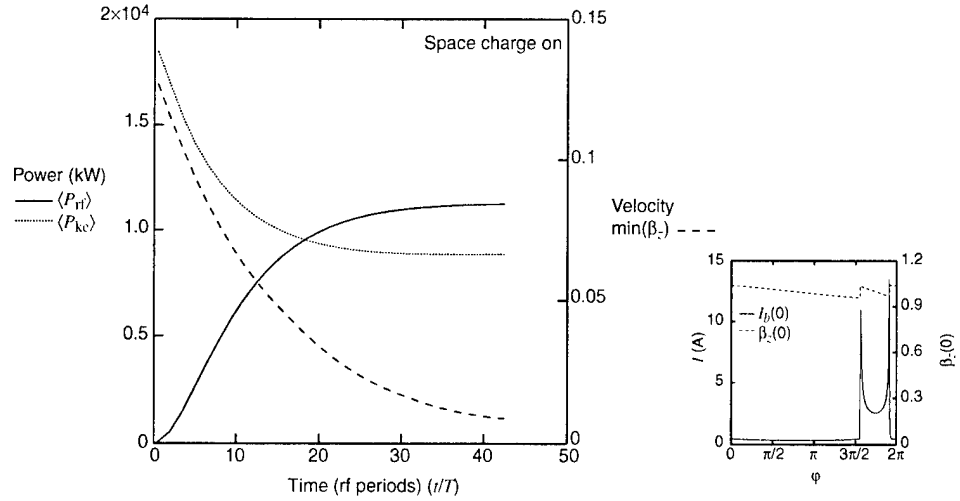


Figure 3. Diagnostics for efficiency-optimized buncher cavity with sinusoidal velocity-modulated 20-kW beam. Rf power is 11.311 kW.

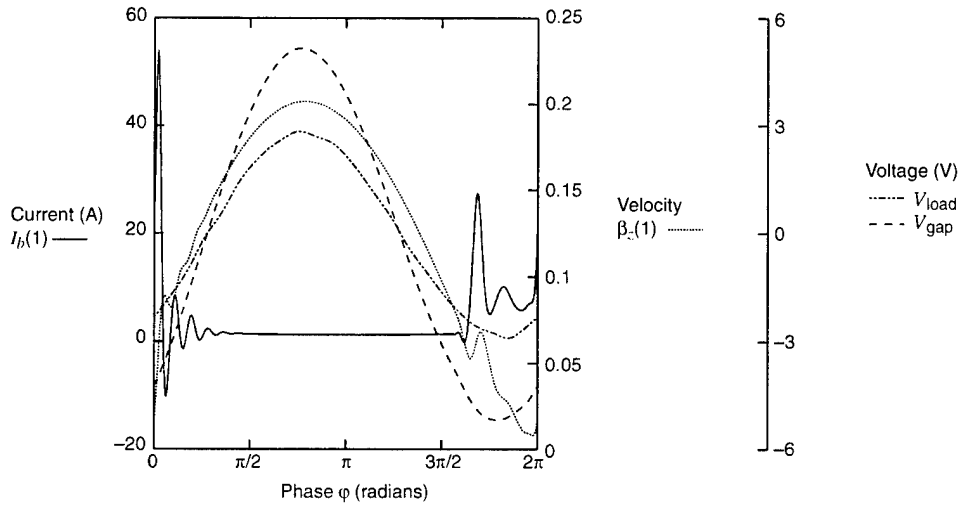


Figure 4. Power convergence for 2-MW beam with sinusoidal velocity modulation. Equilibrium efficiency is $\eta = 0.565$.

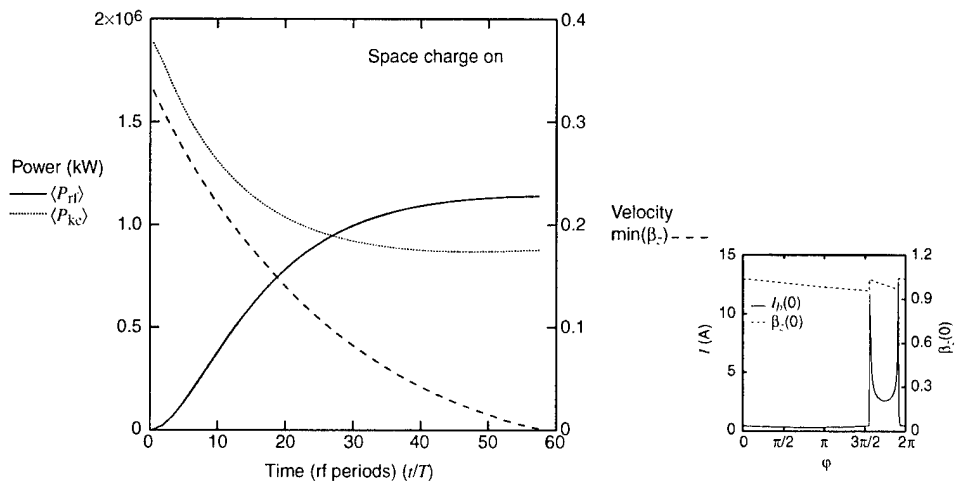


Figure 5. Diagnostics for efficiency-optimized buncher cavity with sinusoidal velocity-modulated 2-MW beam. Rf power is 1113 kW.

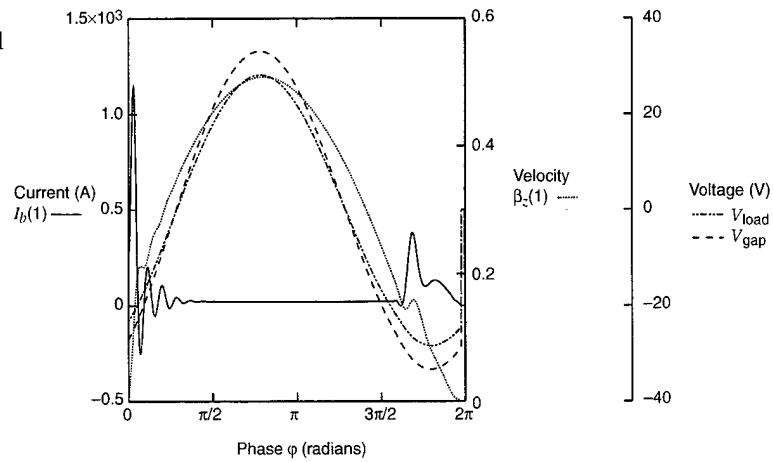


Figure 6. Power convergence for 20-kW beam with 25 percent duty factor gate current modulation. Equilibrium efficiency is $\eta = 0.894$.

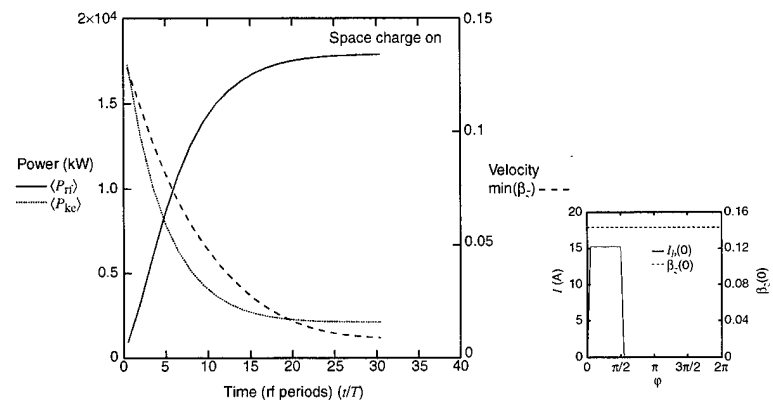


Figure 7. Diagnostics for efficiency-optimized buncher cavity with 25 percent duty factor current-modulated 20-kW beam. Rf power is 17.944 kW.

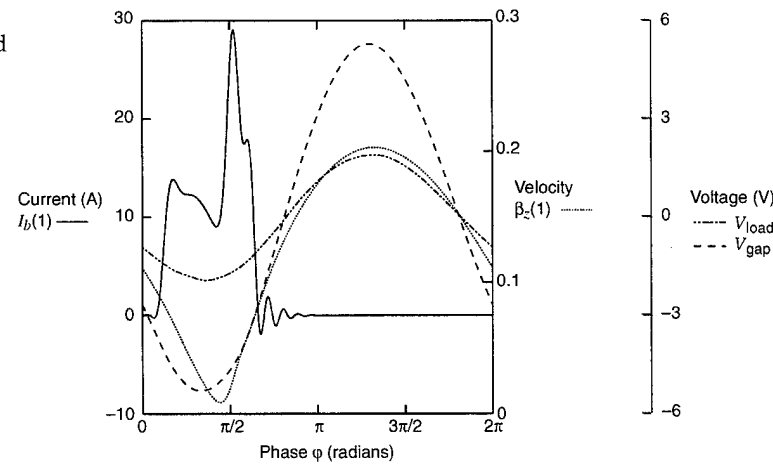


Figure 8. Power convergence for 2-MW beam with 25 percent duty factor gate current modulation. Equilibrium efficiency is $\eta = 0.896$.

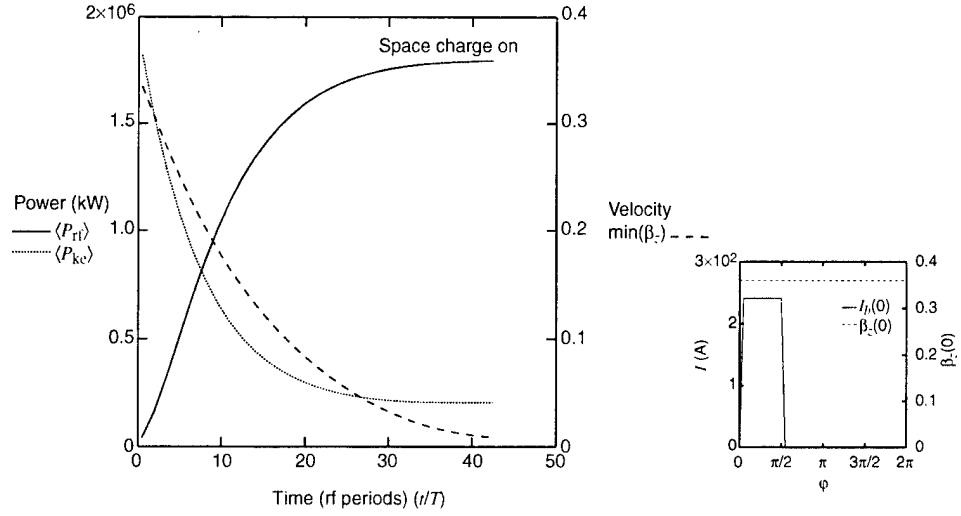
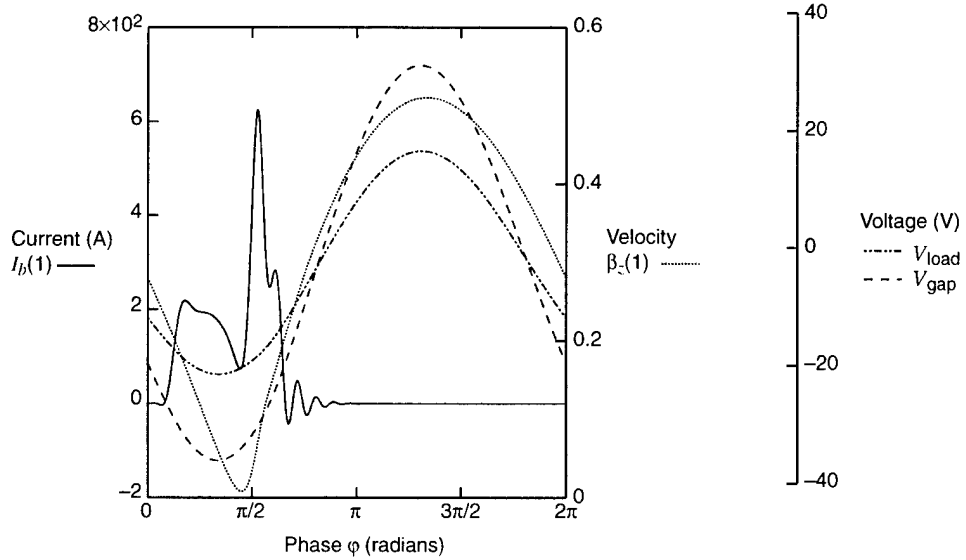


Figure 9. Diagnostics for efficiency-optimized buncher cavity with 25 percent duty factor current-modulated 2-MW beam. Rf power is 1802 kW.



3. Efficiency Enhancement by Harmonic Bunching

3.1 Current Modulation for Arbitrary Velocity Modulation

To determine the velocity modulation required to generate an efficient current modulation, one must develop a way to calculate the current modulation produced by an arbitrary velocity modulation. One way is to use an analytic method based on the ballistic transport equations (74) and (75):

$$t = t_0 + \frac{z}{u_0(t_0)}, \quad \text{and} \quad (74)$$

$$\rho(z, t) = \frac{\rho_0(t_0)}{1 - zu'_0/u_0^2}. \quad (75)$$

The problem with this approach is the multivalued nature of the function that maps electrons at the input of the drift section to electrons at the output of the drift section (electrons with many different input phases can have identical output phases). Another way to calculate the current modulation that is simple but effective is to divide the input phases of the electrons entering the drift region into N^{in} uniform phase intervals and the output phases into N^{out} uniform phase intervals so that

$$\Delta\varphi^{\text{in}} = \frac{2\pi}{N^{\text{in}}}, \quad (76)$$

$$\Delta\varphi^{\text{out}} = \frac{2\pi}{N^{\text{out}}}, \quad (77)$$

$$\varphi_l^{\text{in}} = l\Delta\varphi^{\text{in}}, \quad \text{and} \quad (78)$$

$$\varphi_l^{\text{out}} = l\Delta\varphi^{\text{out}}. \quad (79)$$

In equation (74), t is the time that an electron requires to propagate a distance z if it enters the system ($z = 0$) at time t_0 and with velocity $u_0(t_0)$. Equation (75) relates the charge density contribution at location z and time t , $\rho(z, t)$, to the charge density, $\rho_0(t_0)$, of the electrons entering the system at time t_0 .

I can use equation (74) to map the phase grid defined by equation (78) into a grid of output phases for a drift distance of z . The required phase mapping

$\Phi(\varphi)$ is calculated by renormalizing equation (74) to get (remember that $\varphi = \omega t$, where ω is the modulation frequency)

$$\Phi(\varphi) = \varphi + k_0 z \left(\frac{1}{\beta(\varphi)} - \frac{1}{\beta(0)} \right). \quad (80)$$

In equation (80), k_0 is the wave number of the modulation frequency ($k_0 = \omega/c$), z is the drift distance ($k_0 z$ is dimensionless), and $\beta(\varphi)$ is the normalized velocity modulation $\beta(\varphi) = u_0(\varphi)/c$. Since $\beta(2\pi) = \beta(0)$, I have $\Phi(2\pi) = \Phi(0)$. Please note that having the endpoints of the interval map into themselves does not imply that the interior points of the input phase interval will map into interior points of the output phase interval. However, if a point interior to the input phase interval maps to a point exterior to the output phase interval, there will always be a corresponding point exterior to the input phase interval that will map to a point interior to the output phase interval. Because of the periodic nature of $\Phi(\varphi)$, the point exterior to the input interval will be related to the original point interior to the input interval by a modulus of 2π . Now I denote

$$\Phi_l = \Phi(\varphi_l^{\text{in}}), \quad \text{and} \quad (81)$$

$$\Delta\Phi_l = \left| \Phi(\varphi_{l+1}^{\text{in}}) - \Phi(\varphi_l^{\text{in}}) \right|. \quad (82)$$

The relative current modulation can now be calculated for the output phases φ_l^{out} as follows:

1. Initialize a relative current modulation array \tilde{J}_l^{out} , $0 \leq l < N^{\text{out}}$ to zero.
2. Calculate the output phase array Φ_l , $0 \leq l < N^{\text{in}}$.
3. Determine if any of the output current density phases φ_n^{out} lie in the phase interval $[\Phi_{l+1}, \Phi_l]$.
4. For those φ_n^{out} in the interval $[\Phi_{l+1}, \Phi_l]$, add $\Delta\varphi^{\text{in}}/\Delta\Phi_l$ to the corresponding \tilde{J}_l^{out} .
5. If any part of the interval $[\Phi_{l+1}, \Phi_l]$ is outside the interval $[0, 2\pi)$, bring it inside the interval $[0, 2\pi)$ by translating modulo 2π .
6. Then test the translated interval as in step 3 with any appropriate φ_n^{out} being treated as in step 4.
7. Repeat steps 3 through 6 for all remaining mapped phase intervals $[\Phi_{l+1}, \Phi_l]$.

This procedure automatically accounts for the mapping of multiple input phases to a single output phase. The expression $\Delta\varphi^{\text{in}}/\Delta\Phi_l$ in step 4 results from the requirement of charge conservation in the system.

The first test of this procedure will be for a simple sinusoidal velocity variation of the form

$$\beta(\varphi) = \langle \beta \rangle (1 + \delta \sin(\varphi)), \quad (83)$$

where the optimum drift distance z_0 satisfies the standard klystron relationship for the optimum bunching parameter χ [3, p 305]:

$$\chi = \frac{z_0 k_0 \delta}{\langle \beta \rangle} = 1.84. \quad (84)$$

The results of the procedure are shown in figure 10 for the beam and simulation parameters in table 2.

The current modulation waveform shown in figure 10 is in agreement with those shown in the standard references [3, p 303].

Figure 10. Current modulation for electron beam with sinusoidal velocity modulation at $z = 0.7, 0.8, 0.9$, and 1.0 of optimum drift distance z_0 .

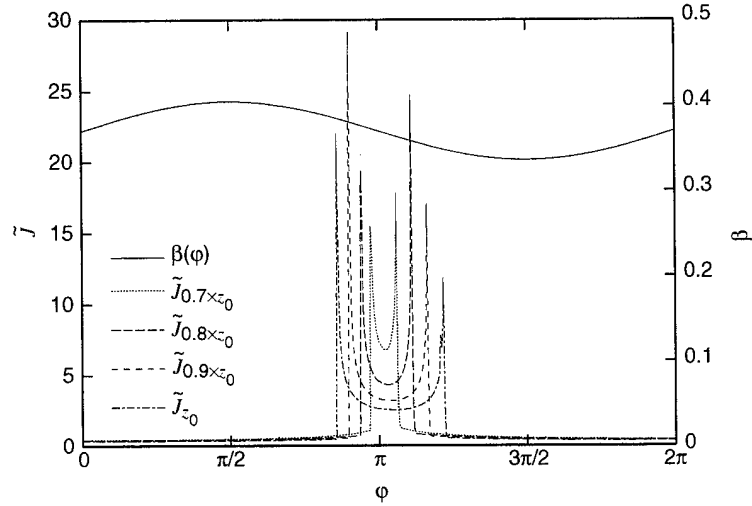


Table 2. Parameters for bunching calculations.

Variable	Value
E_0	35 keV
f_0	1 GHz
z_0	35 cm
$\langle \beta \rangle$	0.37
$k_0 z_0$	7.33
N^{in}	256
N^{out}	1024

3.2 Optimized Velocity Modulation

One can determine the optimum velocity modulation waveform for ballistic bunching by examining equation (75). In dimensionless form, the bunching equation is

$$\frac{\rho(z, \varphi^{\text{out}})}{\rho_0(\varphi^{\text{in}})} = \frac{1}{1 - z k_0 \frac{\beta'(\varphi^{\text{in}})}{\beta^2(\varphi^{\text{in}})}} , \quad (85)$$

with φ^{out} given by equation (80). If optimum ballistic bunching is defined as a repetitive delta function current modulation at frequency ω , the requirement is that all input phases φ^{in} are mapped to a single output phase for each rf cycle for a given $z = z_0$. This condition is met if the denominator on the r.h.s. of equation (85) is zero for all $\varphi^{\text{in}} \in [0, 2\pi]$, so that the defining equation for optimum velocity modulation is

$$1 - z_0 k_0 \frac{\beta'(\varphi^{\text{in}})}{\beta^2(\varphi^{\text{in}})} = 0 . \quad (86)$$

The solution to equation (86) is

$$\beta(\varphi^{\text{in}}) = \frac{\beta(0)}{1 - \frac{\beta(0)}{z_0 k_0} \varphi^{\text{in}}} . \quad (87)$$

To compare different types of velocity modulation, I wish to parameterize them in terms of the average drift velocity $\langle\beta\rangle$ and some modulation index δ . For sinusoidal modulation (eq (83)), the modulation is simply characterized by $\langle\beta\rangle$ and δ , where $\delta = 1.84 \langle\beta\rangle / z_0 k_0$. For optimized velocity modulation, the situation is more complicated. I must integrate equation (87) from 0 to 2π to compute $\langle\beta\rangle$ and then solve the resulting equation for $\beta(0)$, which is then back substituted into equation (76) for elimination. If one defines δ to be

$$\delta = \frac{2\pi \langle\beta\rangle}{z_0 k_0} , \quad (88)$$

the optimum velocity modulation function becomes

$$\beta(\varphi^{\text{in}}) = \frac{\langle\beta\rangle}{\delta} \frac{1 - e^{-\delta}}{1 - (1 - e^{-\delta}) \frac{\varphi^{\text{in}}}{2\pi}} . \quad (89)$$

For the beam and simulation parameters in table 2, the result of the optimum bunching calculation is shown in figure 11. The delta function behavior of the optimized velocity modulation as $z \rightarrow z_0$ is clearly shown in figure 11. The main problem associated with the optimum velocity modulation is determining a way to produce it. Since velocity modulation is

usually imparted to an electron beam, by having the beam transverse a driven oscillating cavity, one is limited to a sinusoidal velocity modulation. One solution is to have multiple bunching cavities driven at frequencies ω , 2ω , 3ω , etc, and perform a Fourier synthesis to approximate the optimum velocity modulation. Figure 12 shows the current density modulation produced by a two-term Fourier approximation (ω and 2ω modulation terms present) at the optimum drift length for the exact optimum velocity modulation. From figure 12, it is not obvious why such a modulation waveform would be an improvement over the optimum sinusoidal waveform shown in figure 10. One can argue why the second harmonic bunching waveform is superior by comparing the two current modulation waveforms for those phases where the current is small. This comparison is made in figure 13, where the \tilde{J} axis has been expanded to accentuate the difference between \tilde{J}_{\sin} and $\tilde{J}_{\text{opt}[2]}$. For $\varphi \notin [3\pi/4, 5\pi/4]$, $\tilde{J}_{\text{opt}[2]} \approx 1/2 \tilde{J}_{\sin}$. If the electrons entering the klystron output cavity are classified according to their entrance phase, approximately half the phases are accelerated and half are deaccelerated. The efficiency of the output cavity is critically dependent on minimizing the total kinetic energy (per rf cycle) imparted to the electrons and on maximizing the total kinetic energy extracted from the electrons. One would expect that during half an rf cycle, electrons would be deaccelerated and during the other half, accelerated. During the accelerated part of the rf cycle, $\tilde{J}_{\text{opt}[2]}$ (fig. 13) would contain half as many electrons as the \tilde{J}_{\sin} bunching waveform. I will now use the output cavity model developed in section 2 to quantitatively evaluate the properties of each modulation waveform.

Figure 11. Current modulation for electron beam with optimized velocity modulation at $z = 0.7, 0.8, 0.9$, and 0.99 of optimum drift distance z_0 .

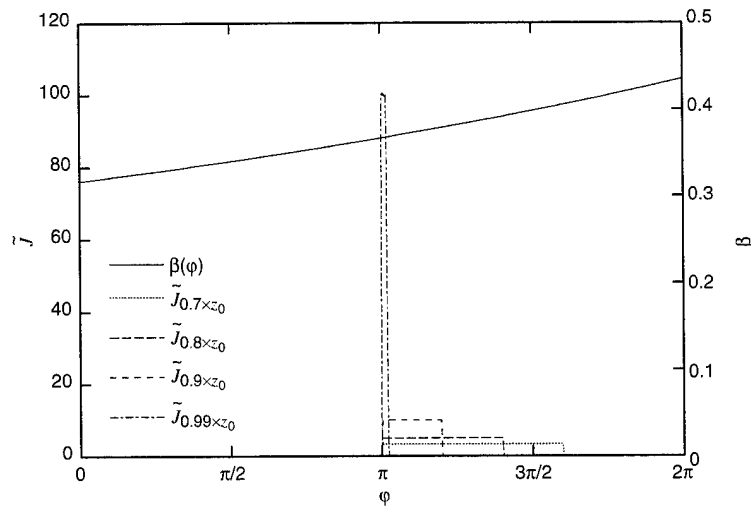


Figure 12. Current modulation for electron beam with second harmonic approximation $\beta_{[2]}(\varphi)$ to optimized velocity modulation at drift length z_0 .

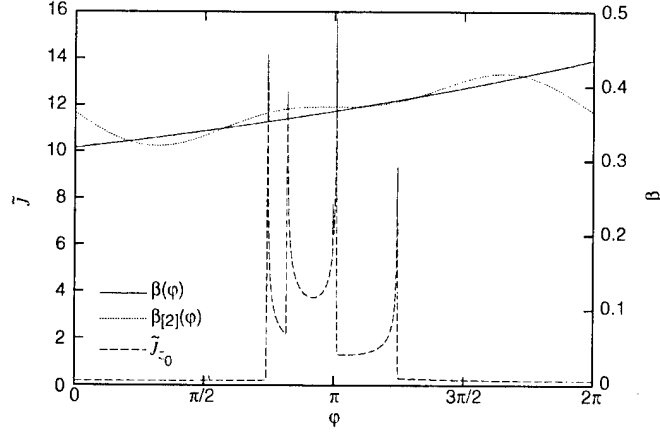
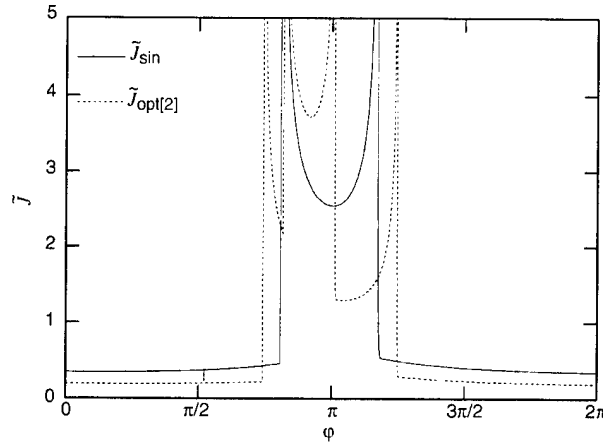


Figure 13. Comparison of current modulation at z_0 for sinusoidal velocity modulation \tilde{J}_{\sin} and second harmonic approximation to optimized velocity modulation $\tilde{J}_{\text{opt}[2]}$.



3.3 Effect of Harmonic Bunching Upon Output Cavity Efficiency

The results of driving a simple (single) output cavity with the current modulation derived from a second harmonic approximation to the optimum velocity modulation are shown in figures 14 to 17. Both 20-kW and 2-MW electron beams are simulated. Figures 14 and 16 show both the input beam current and velocity modulations ($I_b(0)$ and $\beta_z(0)$ in the small graph on the right side of the figures), the average (over one rf cycle) rf power $\langle P_{\text{rf}} \rangle$, and beam kinetic power $\langle P_{\text{ke}} \rangle$, and the minimum value of the velocity field in the cavity gap during the rf cycle, $\min(\beta_z)$. Figures 15 and 17 show the detailed behavior of the beam current $I_b(1)$ and beam velocity $\beta_z(1)$ modulation at the output of the cavity gap. Additionally, the voltages across both the load, V_{load} , and cavity gap, V_{gap} , are shown. The results of the simulations shown in figures 14 to 17 are summarized in table 3.

Note that since the second harmonic ballistic bunching is approximate to the ideal ballistic velocity modulation shown in figure 11, the optimum bunching distance for the second harmonic approximation may not be the distance implicitly defined by equation (88). For the simulations in figures 14 to 17, the parameter z/z_0 was varied in value near 1, until the rf conversion efficiency was maximized. Table 3 shows that using the second harmonic approximation $\beta_{[2]}(\varphi)$ to the ideal bunching velocity modulation yields a significant increase in the klystron output cavity rf conversion efficiency for both the 20-kW and 2-MW electron beams. The explanation for this is evident from the comparison of figures 15 and 3 (20-kW beam) or figures 17 and 5 (2-MW beam). In comparing the beam velocity $\beta_z(1)$ and current $I_b(1)$ at the exit of the output cavity for sinusoidal velocity modulation \tilde{J}_{\sin} (figs. 3 and 5) versus second harmonic velocity modulation $\tilde{J}_{\text{opt}[2]}$ (figs. 15 and 17), the major difference is in the value of beam current outside of the main current bunch. The exit velocity of the beam for the two types of modulation is quite comparable (maximum value, minimum value, and alignment with respect to current bunch); however, the beam current outside of the current bunch is significantly lower for the second harmonic velocity modulation. Since this is the phase region (φ) where the beam velocity is high (for both modulations), the beam with second harmonic velocity modulation will exit the output cavity with significantly less kinetic power than the optimum sinusoidal velocity modulation. Thus, the second harmonic velocity modulation will give a significantly higher rf.

Figure 14. Power convergence for 20-kW beam with optimized second harmonic velocity modulation and output cavity gap located at $z = z_0$. Equilibrium efficiency is $\eta = 0.713$.

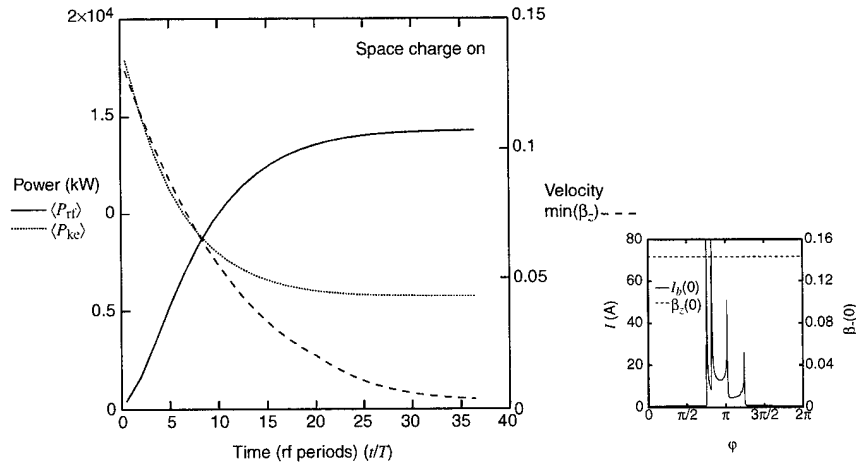


Figure 15. Diagnostics for efficiency-optimized buncher cavity with optimized second harmonic velocity-modulated 20-kW beam and output cavity gap located at $z = z_0$. Conserved power is $\langle P_{rf} \rangle + \langle P_{ke} \rangle = 20.04$ kW.

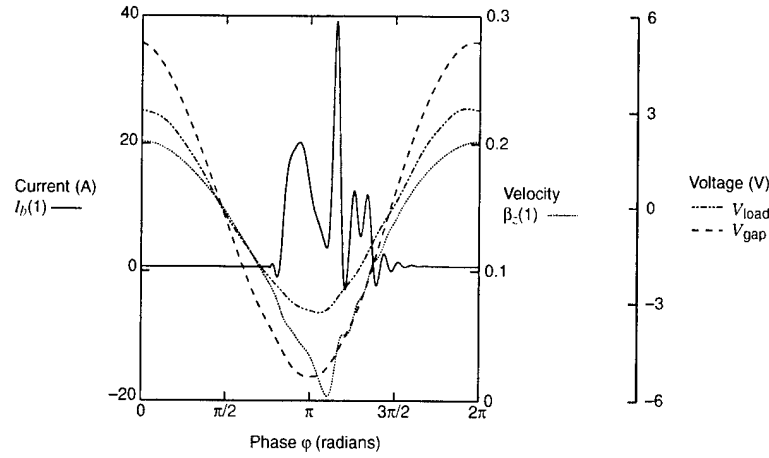


Figure 16. Power convergence for 2-MW beam with optimized second harmonic velocity modulation and output cavity gap located at $z = 0.9z_0$. Equilibrium efficiency is $\eta = 0.706$.

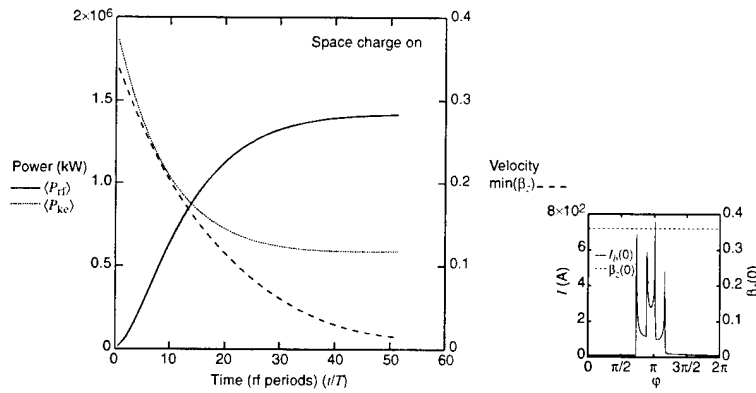


Figure 17. Power convergence for 20-kW beam with optimized second harmonic velocity modulation and output cavity gap located at $z = 0.9z_0$. Conserved power is $\langle P_{rf} \rangle + \langle P_{ke} \rangle = 2003$ kW.

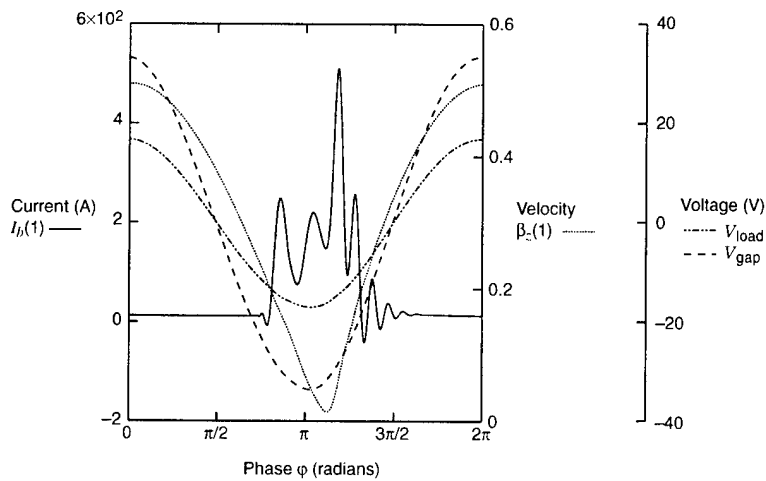


Table 3. Summary of output cavity simulation results for 10- μ perv electron beam with second harmonic ballistic bunching.

Modulation	Beam power	Cavity position	Efficiency	Efficiency increase*	Power error†
2nd harmonic	20 kW	15 cm (z_0)	0.713	0.153	+0.20%
2nd harmonic	2 MW	27 cm ($0.9z_0$)	0.706	0.141	+0.15%

*The efficiency increase is with respect to simple sinusoidal velocity modulation.

†The maximum percent value of $(\langle P_{rf} \rangle + \langle P_{ke} \rangle) / P_{beam} - 1$. This value indicates the degree to which fluid simulation does not conserve energy because of various numerical errors.

4. Conclusions

I have presented an efficient fluid model for the output cavity of a klystron, tested the model for both realistic and optimized beam bunching, derived the optimum velocity modulation for ballistic bunching, derived a realistic approximation to optimum velocity modulation, and compared the operation of a klystron output cavity for optimized sinusoidal velocity beam modulation with that for optimized second harmonic velocity beam modulation. I have shown that optimized second harmonic velocity beam modulation will significantly enhance the rf conversion efficiency of the klystron output cavity at the cost of a more complex beam bunching system (in the simplest case, two driven buncher cavities instead of one).

In general, I have developed an efficient method of performing a first order self-consistent optimization of the klystron output cavity. Specifically, I can calculate the cavity parameters (for a given electron beam and beam modulation), such as loaded Q (in my analysis, I determine the rf load and the cavity gap gain), that would maximize the rf conversion efficiency. This analysis would be the starting point of a multilevel approach for the design of a klystron. The next step would be to verify the fluid optimization with a parametric (cavity modes are given) PIC code. The design would be then optimized with the parametric PIC code. The final design level would be to simulate the improved optimization with a full finite difference time domain (FDTD) PIC code, such as MAGIC or ICEPIC, before any hardware is fabricated.

References

1. A. Bromborsky, "The Multiplet Cavity: A Buncher for Broad-Bandwidth Klystron Amplifiers," *IEEE Trans. Plasma Sci.* **24**, No. 3 (June 1996), pp 928–934.
2. W. H. Press, S. A. Teukolsky, W. T. Vetterling, and B. P. Flannery, *Numerical Recipes in C—Second Edition*, Cambridge University Press, New York, NY (1992).
3. J. W. Gewartowski and H. A. Watson, *Principles of Electron Tubes*, D. Van Nostrand Company, Inc., Princeton, NJ (1965).

Distribution

Admnstr
Defns Techl Info Ctr
Attn DTIC-OCP
8725 John J Kingman Rd Ste 0944
FT Belvoir VA 22060-6218

Ofc of the Secy of Defns
Attn ODDRE (R&AT)
The Pentagon
Washington DC 20301-3080

Ofc of the Secy of Defns
Attn OUSD(A&T)/ODDR&E(R) R J Trew
3080 Defense Pentagon
Washington DC 20301-7100

AMCOM MRDEC
Attn AMSMI-RD W C McCorkle
Redstone Arsenal AL 35898-5240

Dir for MANPRINT
Ofc of the Deputy Chief of Staff for Prsnl
Attn J Hiller
The Pentagon Rm 2C733
Washington DC 20301-0300

SMC/CZA
2435 Vela Way Ste 1613
El Segundo CA 90245-5500

TACOM Rsrch, Dev, & Engrg Ctr
Attn G Kahlil
Attn T Burke
PO Box 249
Warren MI 48090-0249

US Army ARDEC
Attn AMSTA-AR-TD M Fisette
Bldg 1
Picatinny Arsenal NJ 07806-5000

US Army CECOM RDEC
Attn AMSEL-RD-IE-DS-EC R Troisio
Attn AMSEL-RD-NV-OD R Irwin
Attn J Swartz
Bldg 2705
FT Monmouth NJ 07703-5206

US Army Info Sys Engrg Cmnd
Attn AMSEL-IE-TD F Jenia
FT Huachuca AZ 85613-5300

US Army Natick RDEC Acting Techl Dir
Attn SBCN-T P Brandler
Natick MA 01760-5002

US Army Simulation, Train, & Instrmntn
Cmnd
Attn AMSTI-CG M Macedonia
Attn J Stahl
12350 Research Parkway
Orlando FL 32826-3726

US Army Soldier & Biol Chem Cmnd Dir of
Rsrch & Techlgy Dirctr
Attn SMCCR-RS I G Resnick
Aberdeen Proving Ground MD 21010-5423

US Army Tank-Automtv Cmnd Rsrch, Dev, &
Engrg Ctr
Attn AMSTA-TR J Chapin
Warren MI 48397-5000

US Army Train & Doctrine Cmnd
Battle Lab Integration & Techl Dirctr
Attn ATCD-B
FT Monroe VA 23651-5850

US Military Academy
Mathematical Sci Ctr of Excellence
Attn MDN-A LTC M D Phillips
Dept of Mathematical Sci Thayer Hall
West Point NY 10996-1786

Cmnd Ofcr Nav Rsrch Lab
Attn Code 6843 D Abe
Attn Code 6793 S Gold
Attn Code 6841 B Levush
Attn Code 6843 B Danly
4555 Overlook Ave SW
Washington DC 20375-5320

Nav Surface Warfare Ctr
Attn Code B07 J Pennella
17320 Dahlgren Rd Bldg 1470 Rm 1101
Dahlgren VA 22448-5100

US Air Force Phillips Lab
Attn J O'Loughlin
Attn K Hackett
3550 Aberdeen Ave SE
Kirtland Air Force Base NM 87112-5776

Distribution (cont'd)

DARPA
Attn S Welby
3701 N Fairfax Dr
Arlington VA 22203-1714

Univ of Maryland
Energy Rsrch Facility
Attn G Nusinovich
Attn S Vlasov
Attn V Granatstein
College Park MD 20742-3511

Hicks & Associates Inc
Attn G Singley III
1710 Goodrich Dr Ste 1300
McLean VA 22102

Mission Rsrch Corp
Attn M Bollen
Attn R Smith
Attn J Pasour
8560 Cinderbed Rd Ste700
Newington VA 22122

NorthStar Rsrch
Attn R Richter-Sand
Attn R Adler
4421 A McLeod NE
Albuquerque NM 87109

Palisades Inst for Rsrch Svc Inc
Attn E Carr
1745 Jefferson Davis Hwy Ste 500
Arlington VA 22202-3402

Director
US Army Rsrch Ofc
Attn AMSRL-RO-D JCI Chang
PO Box 12211
Research Triangle Park NC 27709

US Army Rsrch Lab
Attn AMSRL-DD J M Miller
Attn AMSRL-CI-AI-A Mail & Records Mgmt
Attn AMSRL-CI-AP Techl Pub (3 copies)
Attn AMSRL-CI-LL Techl Lib (3 copies)
Attn AMSRL-SE-D E Scannell
Attn AMSRL-SE-DP A Bromborsky
(25 copies)
Attn AMSRL-SE-DP H Brandt
Attn AMSRL-SE-DP R A Kehs
Attn AMSRL-SE-DP T F Podlesak
Attn AMSRL-SE-DS L Jasper
Attn AMSRL-SE-DS W O Coburn
Attn AMSRL-SE-P M J Plott
Attn AMSRL-SE-RE F Crowne
Attn AMSRL-SE-RE R Chase
Attn AMSRL-SE-RE R del Rosario
Attn AMSRL-WT-NF M Berry
Adelphi MD 20783-1197

REPORT DOCUMENTATION PAGE			Form Approved OMB No. 0704-0188	
Public reporting burden for this collection of information is estimated to average 1 hour per response, including the time for reviewing instructions, searching existing data sources, gathering and maintaining the data needed, and completing and reviewing the collection of information. Send comments regarding this burden estimate or any other aspect of this collection of information, including suggestions for reducing this burden, to Washington Headquarters Services, Directorate for Information Operations and Reports, 1215 Jefferson Davis Highway, Suite 1204, Arlington, VA 22202-4302, and to the Office of Management and Budget, Paperwork Reduction Project (0704-0188), Washington, DC 20503.				
1. AGENCY USE ONLY (Leave blank)		2. REPORT DATE June 2000		3. REPORT TYPE AND DATES COVERED Final, Oct 1998–Sept 1999
4. TITLE AND SUBTITLE Fluid Simulation of Klystron Output Cavities With Optimization of Electron Beam Bunching			5. FUNDING NUMBERS DA PR: A140 PE: 62120A	
6. AUTHOR(S) Alan Bromborsky				
7. PERFORMING ORGANIZATION NAME(S) AND ADDRESS(ES) U.S. Army Research Laboratory Attn: AMSRL-SE-DP email: brombo@arl.mil 2800 Powder Mill Road Adelphi, MD 20783-1197			8. PERFORMING ORGANIZATION REPORT NUMBER ARL-TR-2097	
9. SPONSORING/MONITORING AGENCY NAME(S) AND ADDRESS(ES) U.S. Army Research Laboratory 2800 Powder Mill Road Adelphi, MD 20783-1197			10. SPONSORING/MONITORING AGENCY REPORT NUMBER	
11. SUPPLEMENTARY NOTES ARL PR: 9NEYXX AMS code: 622120.140				
12a. DISTRIBUTION/AVAILABILITY STATEMENT Approved for public release; distribution unlimited.			12b. DISTRIBUTION CODE	
13. ABSTRACT (Maximum 200 words) A one-dimensional fluid model for a coupled system of klystron output cavities is developed. The model is exercised for both realistic and optimized beam current modulation waveforms, and the rf conversion efficiency is calculated. An optimized second harmonic velocity modulation and associated current modulation are calculated and inputted into the cavity simulation. Optimum bunching lengths and rf conversion efficiencies are determined.				
14. SUBJECT TERMS Fluid cavity, bunching optimization			15. NUMBER OF PAGES 41	
			16. PRICE CODE	
17. SECURITY CLASSIFICATION OF REPORT Unclassified	18. SECURITY CLASSIFICATION OF THIS PAGE Unclassified	19. SECURITY CLASSIFICATION OF ABSTRACT Unclassified	20. LIMITATION OF ABSTRACT UL	